

RESEARCH

Open Access



Design and measurement of a 5G mmW mobile backhaul transceiver at 28 GHz

Olli Kursu^{1*} , Marko E. Leinonen¹, Giuseppe Destino¹, Nuutti Tervo¹, Marko Sonkki¹, Timo Rahkonen¹, Aarno Pärssinen¹, Saira Tammelin¹, Marko Pettissalo² and Aki Korvala²

Abstract

High throughput and ultra low latency are the main requirements for fifth generation (5G) mobile broadband communications. Densely populated urban environments require utilization of previously underutilized millimeter wave frequency spectrum for higher data rates. The Ka-band, previously used in satellite applications, is of particular interest to terrestrial 5G mobile networks. New radio solutions are required for these frequencies, such as multiple wireless base stations organized in small cells and highly directional antennas to compensate for higher path loss. Wireless backhaul is predicted to be the most cost-effective and versatile solution to connect 5G base stations to the core network. Wireless backhaul enables flexible and easy installation of 5G base stations in ad hoc networks, supporting large crowd gatherings such as concerts and sports events. In this article, we present an architecture of a wireless backhaul transceiver, which operates on the 26.5–29.5-GHz band. The architecture described in this paper was implemented, and the performance of the receiver (Rx) array has been measured. We also present over-the-air antenna array measurement results using the Rx. The measurement results show that unequal Rx channel gains and antenna gains do not have a significant effect on the shape of the main lobe of the radiation pattern. We have measured a coherence gain of 2.7 dB from two Rx channels that is close to the theoretical value of 3.0 dB. We have achieved a conducted Rx EVM of better than 2% using a 100-MHz 16-QAM modulated signal at 26.5 GHz.

Keywords: 5G, Transceiver, Backhaul, Millimeter wave, Radio frequency, Antenna array, Antenna pattern, Beamforming

1 Introduction

One of the technology drivers of the fifth generation (5G) mobile networks is the communication at the millimeter wave (mmW) frequency bands such as the Ka- and the E-band. The frequency spectrum between 26.5 and 29.5 GHz is proposed to be used for Winter Olympics in South Korea, of which 27.5–28.5 GHz is allocated for proof-of-concept 5G demonstrations [1]. Some prototype designs operating at or close to the aforementioned frequency band have been recently presented in the literature [2–7]. All of them, with the exception of [7] are integrated circuit solutions that do not reach the output power levels required for long-range wireless backhaul. Future 5G network base stations for mmW bands will operate at much shorter ranges than current LTE 4G networks, mainly due

to their higher operating frequency. A few hundred meters can be considered as long range for a mobile backhaul operating above 26 GHz. Such ranges require highly adaptive beamforming, highly directional antenna gain and mobility management.

Most probably, 5G systems operating below 40 GHz will utilize orthogonal frequency-division multiplexing (OFDM) waveform with multiple parallel data streams [8]. Multiple input multiple output (MIMO) is enabled by large antenna arrays together with hybrid digital-radio frequency (RF) beamforming. The MIMO-OFDM solution follows a classical implementation of a Long-Term Evolution (LTE) modem including scrambling, quadrature modulation, layer mapping, MIMO precoding, frequency resource mapping, and OFDM signal generation.

We have presented system-level calculations and link budget analysis for a backhauling proof-of-concept radio unit aiming at a > 2 Gbps data rate and a range of 200 m

*Correspondence: Olli.Kursu@oulu.fi

Saira Tammelin, Centre for Wireless Communications, currently with Nokia

¹Centre for Wireless Communications, University of Oulu, Oulu, Finland

Full list of author information is available at the end of the article

in [9], designed for the 5GChampion trial in conjunction with the 2018 Winter Olympics.

2 Methods

We have built a prototype mmW transceiver based on the Rx and Tx system-level calculations and simulations. We have simulated the transmission lines and impedance matchings of the implemented printed circuit board (PCB) using a 2.5D EM simulator. We present conductive measurements with continuous wave (CW) and with digitally modulated signals, which verify the functionality and performance of the radio. Digitally modulated wide band signals are used to emulate the operation of the Rx with a real OFDM signal. We have characterized the implemented radio Rx with mmW frequency measurements including coherence gain, dynamic range, and error vector magnitude (EVM) measurements for Rx chains. We have also measured the Rx attenuator linearity.

We have simulated an antenna array with 3D EM simulator and implemented a prototype based on the design. We have measured the radiation pattern of the 2x2 antenna sub-array and calculated the full array pattern using MATLAB. Effect of imbalance between gains of the Rx channels to the gain of the antenna array is analyzed as a final step of the characterization. Power consumption of the transceiver has also been estimated.

3 Overview of the radio system implementation

A block diagram of the implemented transceiver is shown in Fig. 1 [9]. The transceiver is planned to be interfaced to a digital front-end (DFE) that does the baseband processing. The implemented radio system consists of an eight-channel transceiver array. Commercial aluminum gallium arsenide (AlGaAs) P-I-N diode switches (MASW-011036) are used to combine the Rx and transmitter (Tx) paths

to a common antenna port. Antenna switch can be used, since the radio operates in time division duplex (TDD) mode, where Tx and Rx are active at different time slots. On the front-end, eight commercial 9-W power amplifiers (PA) (TGA2595) drive an array of eight sub-arrays each composed by four sub-elements in a 2x2 configuration. Eight commercial low-noise amplifiers (LNA) (MAAL-011111) that have a small signal gain of 19 dB and a noise figure of 2.5 dB are placed in parallel with the PAs. Each PA/LNA pair is preceded by a phase shifter component which has a 5-bit control giving an 11.25° phase resolution. A passive Wilkinson power divider/combiner network is located between the RF front-end and the preamplifiers.

The common path, located behind the power division/combining network, uses the same PA and LNA components for amplification. In order to improve the linearity of the Tx chain, the amplifiers driving the power divider network are biased so that the first preamplifier consumes half the current (280 mA) compared to the final stage PAs driving the antennas (560 mA) and the second preamplifier is biased to the same bias point as the final stage PA. The used PAs are normally on gallium nitride (GaN) devices which require a negative gate bias voltage to turn off the transistor before applying the drain voltage. The gate voltages of the GaN amplifiers are digitally controlled with a DAC that provides the negative voltage bias, so that at start-up the bias, voltage is set to -5 V and can be ramped up to the appropriate bias point during operation and measurements. The drain voltages can also be controlled with an on/off switch, so that they are not accidentally turned on if the negative voltage supply is disconnected at start-up.

A simple on/off control is also implemented for the LNAs. The operating frequency can be set with a commercial frequency synthesizer located on the board and

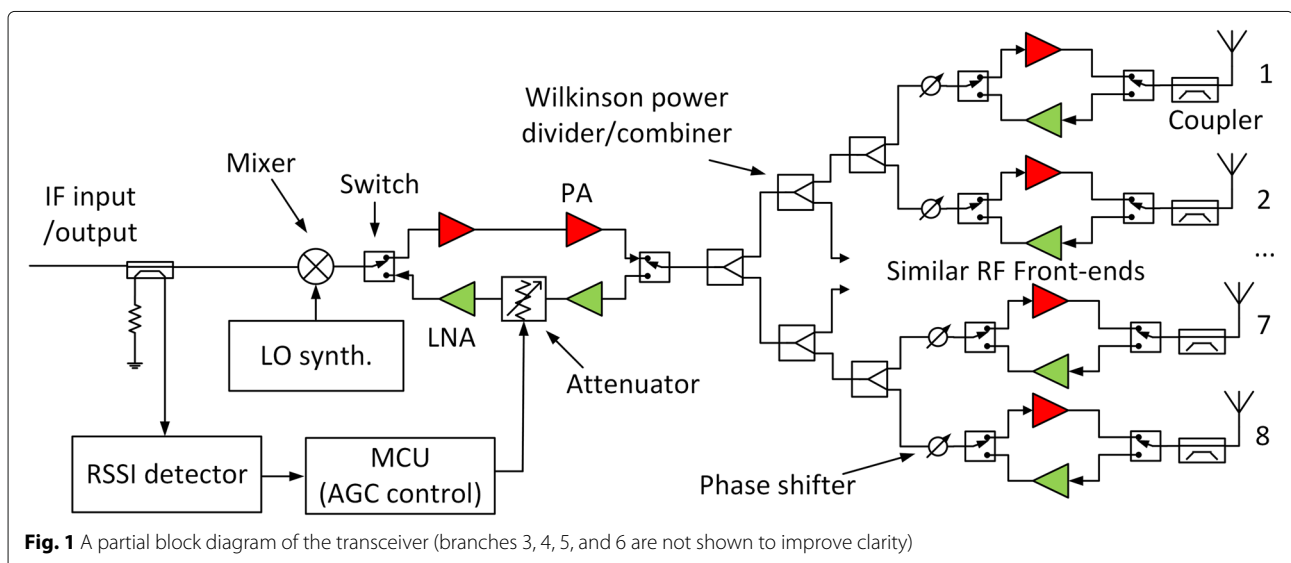


Fig. 1 A partial block diagram of the transceiver (branches 3, 4, 5, and 6 are not shown to improve clarity)

controlled via an Serial Peripheral Interface (SPI) bus. Phase shifters are controlled by shift registers via a second SPI bus. A microcontroller unit (MCU) which also runs an RF beamformer algorithm that calculates the appropriate control words for the phase shifters is used to adjust all the digital controls on the RF board.

A commercial passive subharmonically pumped gallium arsenide (GaAs) mixer that contains an integrated LO amplifier acts as an up and downconverter between the 3–6 GHz intermediate frequency (IF) and the final RF frequency. Subharmonic pumping eases the requirement for the LO synthesizer, allowing us to use a commercial component that has an LO frequency of

$$LO = \frac{RF - IF}{2} \tag{1}$$

The Rx path also contains a commercial logarithmic detector that is used as a part of received signal strength indicator (RSSI) and automatic gain control (AGC). It operates on the IF and is located behind a directional coupler. We have used SMPM connectors for both IF ports and antenna (RF) ports. An antenna module can be connected to the radio board either with short cables or with SMPM-SMPM “bullets” between two SMPM connectors.

3.1 RF board implementation

The PAs are bare die devices and the PCB contains copper “coins” located under each PA which directly connect the PA to the heat sink under the PCB, as shown in Fig. 2. The coin stops in the prepreg substrate, leaving the vertical distance from the top of the coin to the surface of the PCB to about 250 μm. Since the thickness of the die is 100 μm, a step of approximately 100 μm is left from the top of the die to the top of the PCB after the die is soldered on top of the coin. RF switches and phase shifters are also bare die devices and those are placed top of the PCB. A photo

of the designed RF board is shown in Fig. 3. The thickness (127 μm) of the core substrate between the top layer and the ground plane is chosen so that the 50 ohm line width (285 μm) matches the physical pins of the RF components as closely as possible.

Since the selection of commercial components operating at the Ka-band is limited, the reference designs of individual components use different substrate materials and substrate thicknesses, which in turn causes some variation to available pin sizes. Most components have a line width transition from the 285 μm 50 ohm line on the PCB to a 300-μm-wide pin. The Wilkinson power divider has the largest line width transition (to 350 μm), which according to full-wave 2.5D EM simulations causes only a negligible additional loss at 28 GHz. The transmission lines on the PCB are microstrip lines, which are separated from the surface ground plane by a 1-mm clearance.

3.2 Antenna array

The antenna array consists of eight sub-arrays. Each sub-array consists of four linearly polarized patch elements, oriented in – 45° with respect to the vertical. Each patch element within the sub-array is excited with the same amplitude and phase. The structure of a single sub-array is shown in Fig. 4. The sub-array is designed for 28 GHz center frequency with a 10% relative – 10 dB impedance bandwidth. The maximum gain to the broadside direction is 10.8 dB.

A photo of a 2×8 element antenna array is shown in Fig. 5. The part marked by a dotted red line is used in the measurement to form a 1×8 element. Unused antenna elements are terminated with a 50 ohm load. A simulated radiation pattern of an eight sub-array antenna element is shown in Fig. 6. Direction of the beam can be adjusted only in the azimuth plane (Phi).

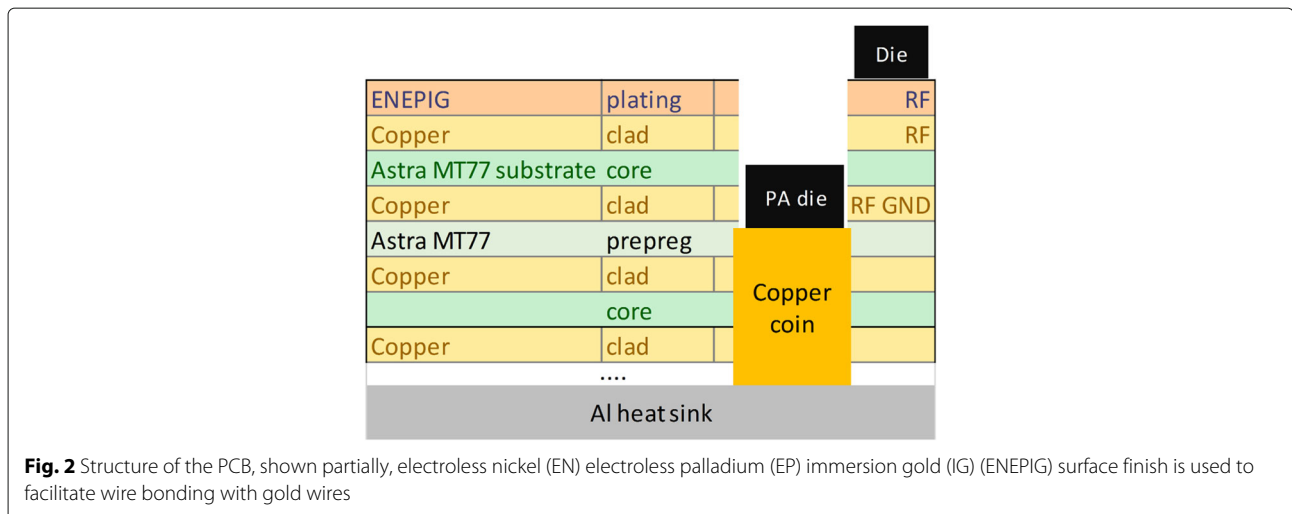


Fig. 2 Structure of the PCB, shown partially, electroless nickel (EN) electroless palladium (EP) immersion gold (IG) (ENEPIG) surface finish is used to facilitate wire bonding with gold wires

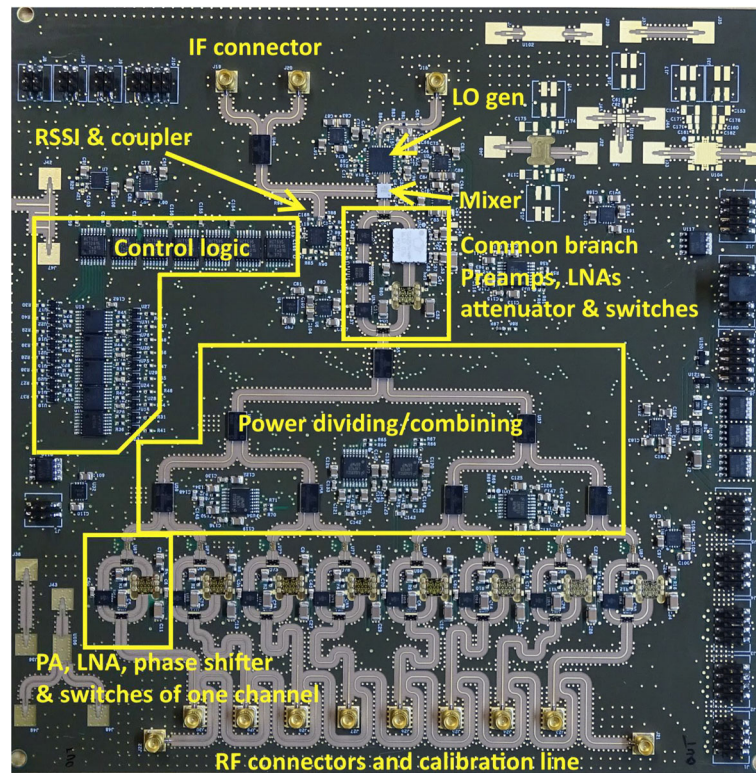


Fig. 3 A photograph of the RF board [9]

4 System and link budget analysis

The cascaded gain and OIP3 of the Tx path and the cascaded gain and noise figure of the Rx path, calculated based on the values given by the component data sheets, are shown in Figs. 7 and 8, respectively [9]. Microstrip losses are included in the analysis, since at the used frequency, they have a noticeable impact on the achievable gain and noise figure. Microstrips are simulated at 28 GHz using a full-wave 2.5D EM simulator. Front-end losses caused by the SMPM connectors and the interface between them is predicted to be around 1.5 dB.

The link budgeted analysis, showing the trade-off between the achievable range and achievable data rate, is shown in Fig. 9 [9]. The SNR requirement for the Rx for different modulations are QPSK = 10 dB, 16-QAM = 18 dB, 64-QAM = 26 dB and 256-QAM = 34 dB. They are based on the model presented in [10]. Coding rate of 0.85 is used. The transmitted power used in the link budget analysis is the effective isotropic radiated power (EIRP), which takes into account both the number of active PAs and the gain of the antenna element. The link budget is plotted for the ideal case and including two different types on

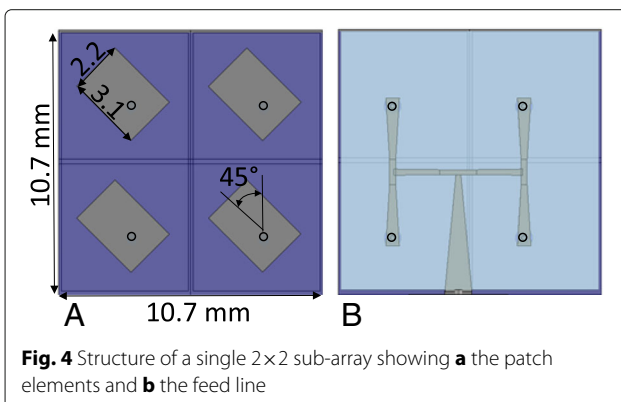


Fig. 4 Structure of a single 2x2 sub-array showing a the patch elements and b the feed line

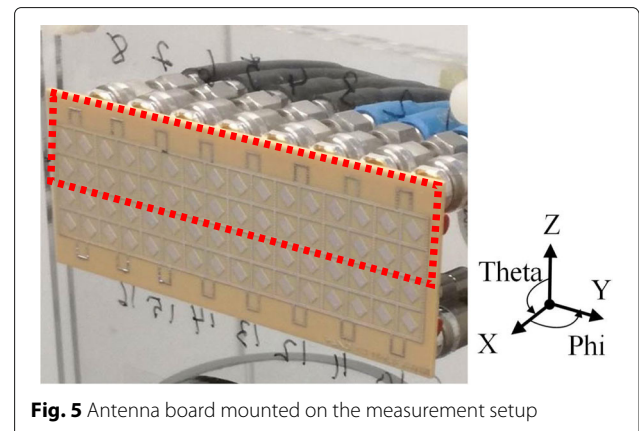


Fig. 5 Antenna board mounted on the measurement setup

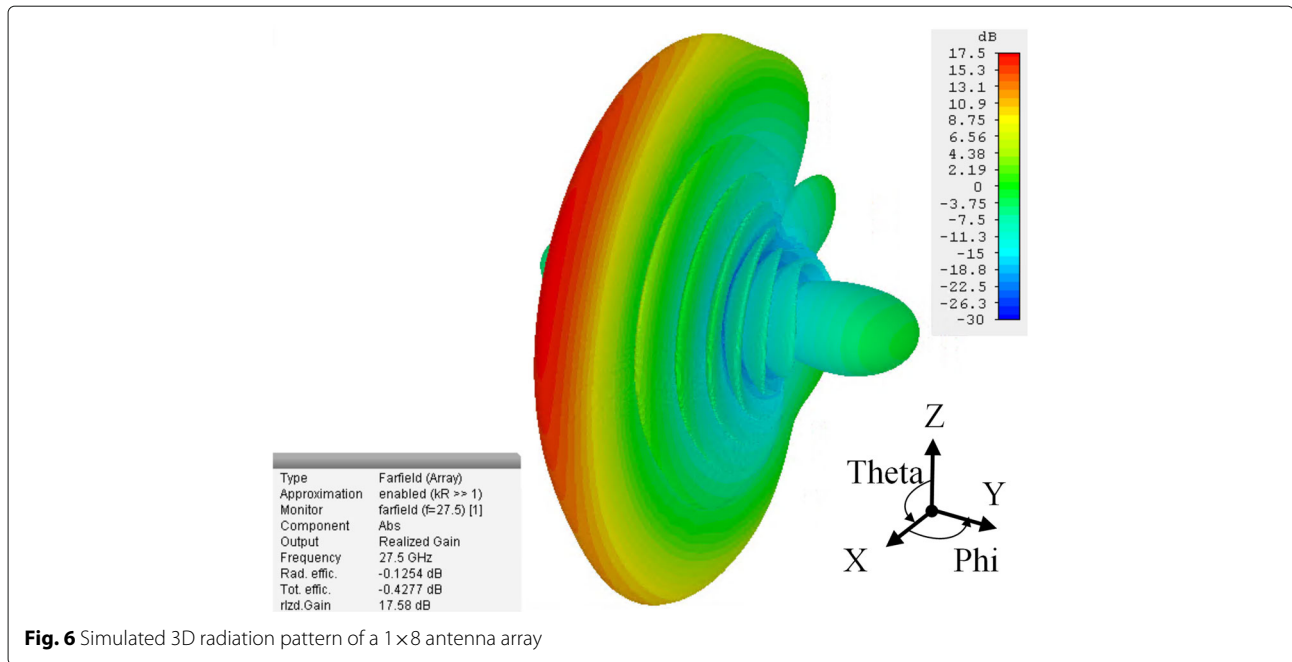


Fig. 6 Simulated 3D radiation pattern of a 1 × 8 antenna array

non-idealities, EVM losses and EVM-Tx FE losses. More realistic models predict a significant loss to the achievable range. It can be seen from Fig. 9 that a 64-QAM signal with a 100-MHz bandwidth is sufficient to achieve the requirement for a 2.5 Gbps link and 200 m coverage [9].

5 Measurement results

A block diagram of the test setup is shown in Fig. 10. Conductive measurements have been done to verify the performance of the radio Rx. Channels that are inactive during measurements have been terminated with a 50 ohm standard load connected to the antenna port.

5.1 Compression curves and coherence gain of the Rx

We have measured the compression behavior of the Rx by power sweeping a 100-MHz-wide digitally modulated input signal at a fixed measurement frequency of 26.5 GHz. The measurement has been carried out by turning one and two Rx channels on at the same time. The results are shown in Fig. 11. Both Rx channels have similar dynamic range and gain compression at high input levels. The coherence gain of an array Rx indicates the quality of the phased array when summing beams from the desired direction. The maximum value for the coherence gain of two signals with equal amplitudes and phases is 3 dB.

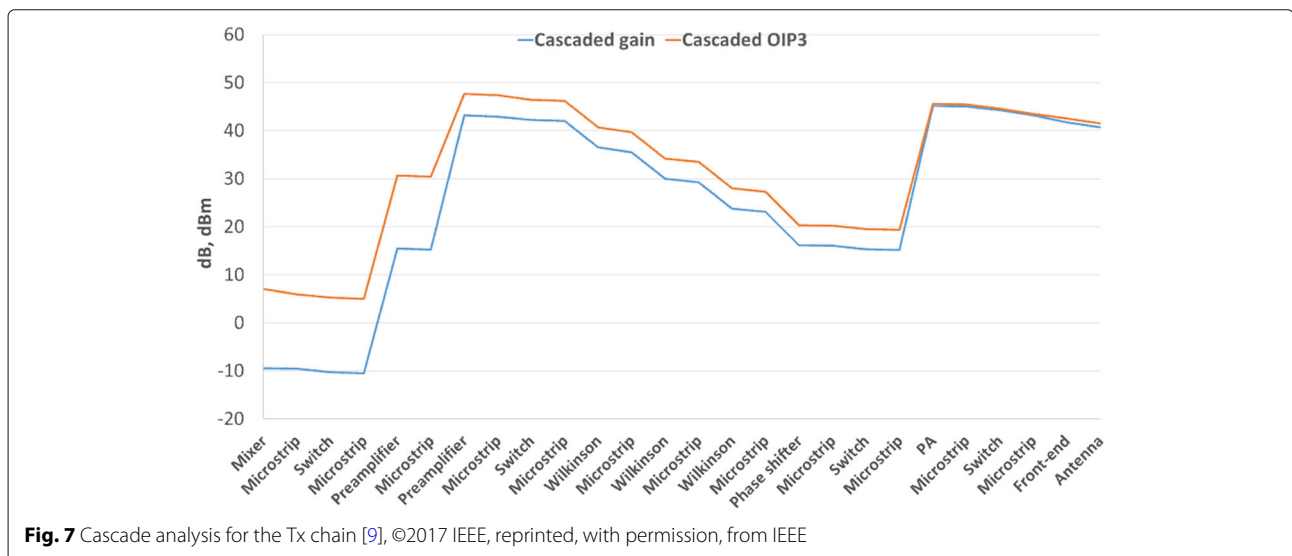


Fig. 7 Cascade analysis for the Tx chain [9], ©2017 IEEE, reprinted, with permission, from IEEE

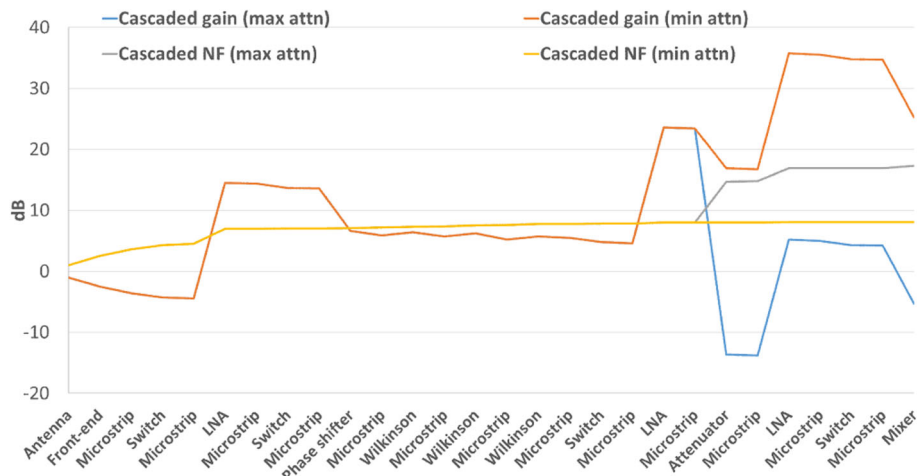


Fig. 8 Cascade analysis for the Rx chain [9], ©2017 IEEE, reprinted, with permission, from IEEE

The maximum signal-to-noise ratio (SNR) is improved by $10\log_{10}(N)$ in an array Rx with N channels [11].

In practice, the coherence gain will be lower due to component and layout non-idealities. Input signal level of -40 dBm with a 16-QAM modulation is fed to both Rxs and the measured output levels from individual Rxs are -35.9 dBm and -36.7 dBm. The power sum of individual output levels is -33.3 dBm; however, the measured combined power is -30.6 dBm. This indicates that the coherence gain between Rxs 3 and 6 is 2.7 dB, which is close to optimum and can be seen from Fig. 11.

Figure 11 also shows that with a 64-QAM modulation using the same bandwidth a smaller coherence gain of 2.2 dB is achieved. This can be partly attributed to the different crest factors of 16-QAM and 64-QAM modulations, which are 2.55 and 3.68 dB, respectively. There is also a 1.2-dB difference in the output signal levels of the 16-QAM and 64-QAM modulations, where 64-QAM has the higher signal level. This difference is caused by the scaling done by the RF equipment, which could have been calibrated out. However, this would not change the coherence gain results.

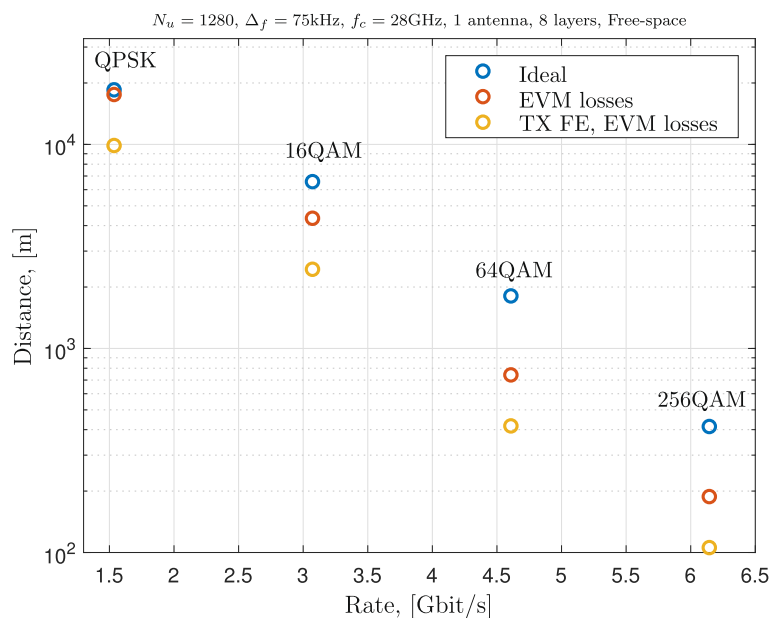


Fig. 9 Link budget analysis for eight layers [9] ©2017 IEEE, reprinted, with permission, from IEEE

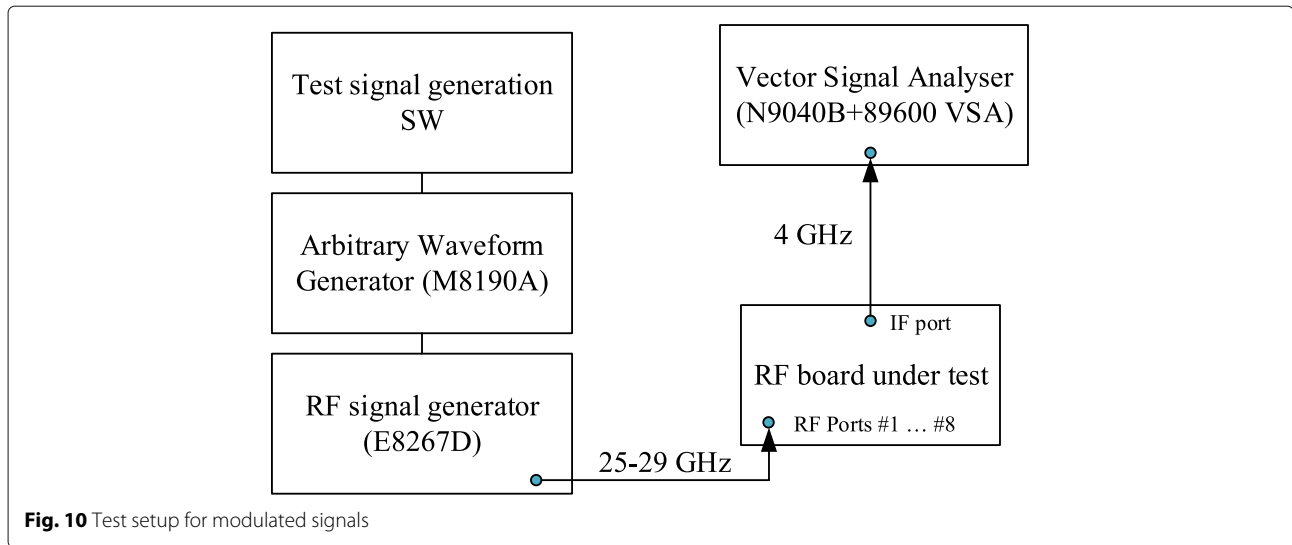


Fig. 10 Test setup for modulated signals

We have also measured coherence gains with signal bandwidths of 200, 400, and 800 MHz using the same Rxs and the 26.5 GHz center frequency. The results are shown in Fig. 12, and a summary of achieved coherence gains is shown in Table 1.

5.2 Linearity of the automatic gain control

The dynamic range of the Rx is limited by the compression of the first front-end LNA and the linearity of the mixer. To extend the dynamic range of the receiver to support mobility, we have implemented AGC functionality using a digitally controllable attenuator. The attenuator has 31 dB dynamic range and can be controlled using a 5-bit parallel input with 1 dB steps. Figure 13 shows a measured sweep through all attenuation states.

The attenuator measurement has been done by feeding a 100-MHz-wide 16-QAM modulated signal at 26.5 GHz

to two Rx channels simultaneously and measuring the output power at the IF port. Measurement results are marked using a solid blue line and the ideal decibel-linear attenuation is shown with a red dotted line. It can be seen from results that the attenuator is not providing linear attenuation on two control states, although the response is still monotonic. A linear attenuation error within the first 10 dB is 1.7 dB, and for a 20 dB range the error is 1.8 dB and for the full 31 dB dynamic range it is 3.1 dB. The AGC functionality can compensate this kind of linear attenuation error by using look-up tables (LUT).

5.3 Error vector magnitude of the Rx

EVM is defined as

$$EVM = \frac{\sqrt{\frac{1}{N} \sum_{n=0}^{N-1} (I_{err}[n]^2 + Q_{err}[n]^2)}}{P_{reff}}, \tag{2}$$

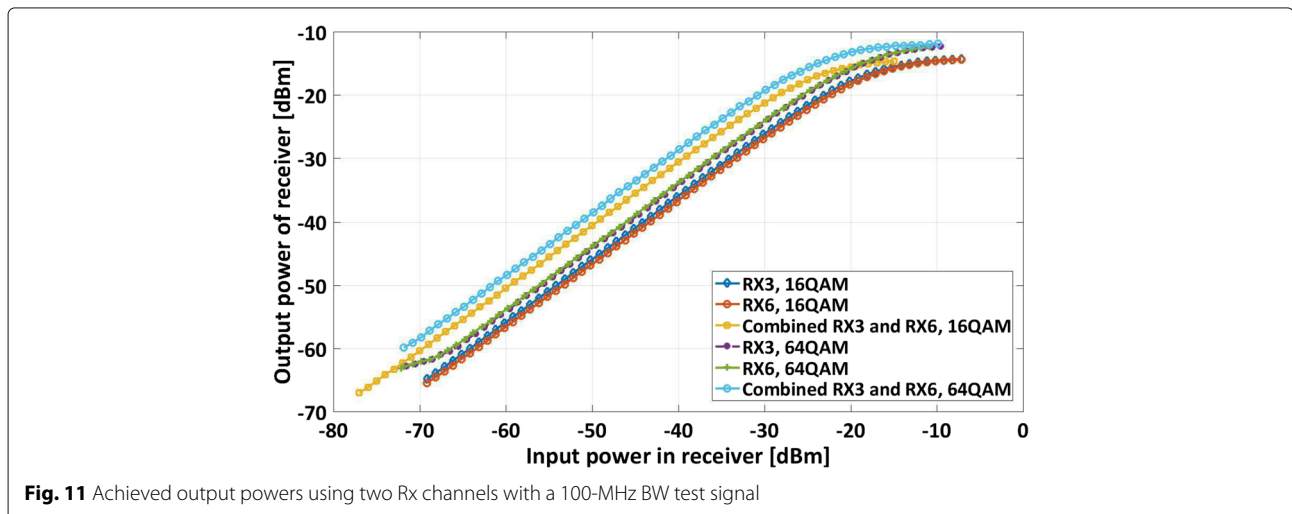


Fig. 11 Achieved output powers using two Rx channels with a 100-MHz BW test signal

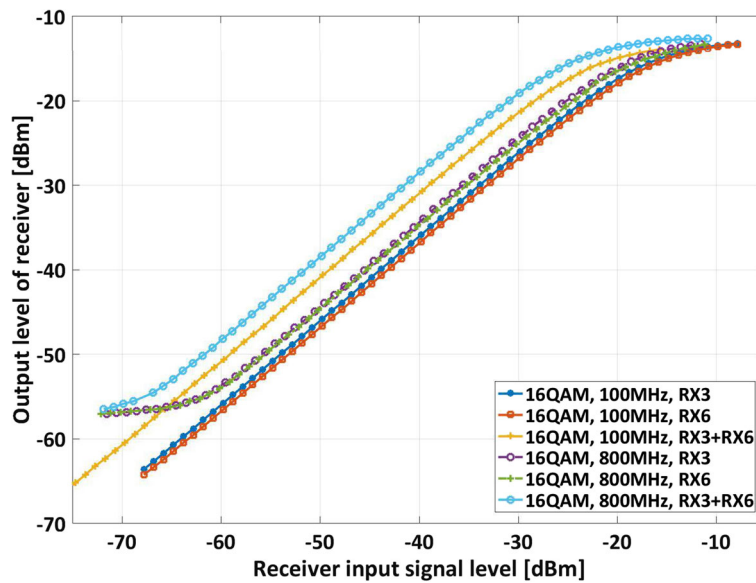


Fig. 12 Achieved output powers using 16-QAM and a varying signal bandwidth

where n is the symbol index, N is the number of symbols, $I_{err} = I_{ref} - I_{meas}$ is an error of the I signal from the reference point and $Q_{err} = Q_{ref} - Q_{meas}$ is an error of the Q signal from the reference point [12]. The EVM and SNR has a relationship according to

$$SNR = -20 \log_{10} \frac{EVM}{100\%}, \tag{3}$$

where EVM is expressed as a percent value. EVM measurements have been conducted to all Rxs individually with a 100-MHz-wide 16-QAM modulated signal at 26.5 GHz, and the input power in the antenna port of each Rx has been swept. The output of the Rx is connected to a vector signal analyzer (VSA) at intermediate frequency (IF). The VSA demodulates the signal and calculates the EVM. The results are presented in Fig. 14.

There is an optimum minimum point on the EVM curve where the SNR is maximized. EVM deteriorates with high input power levels due to the compression of the first LNA. At low signal levels, thermal noise limits the available SNR. It can be seen from Fig. 14 that three Rxs (2, 8, and 5) do not perform as well as the others.

Table 1 Coherence gains using 16-QAM modulation

	100 MHz	200 MHz	400 MHz	800 MHz
Coherence gain (dB)	2.7	2.1	2.3	2.6

5.4 Amplitude imbalance effect on the gain of the Rx array

A phased array transceiver ideally has similar small signal gains in all Rx and Tx channels for minimizing the noise figure in the Rx and maximizing the EIRP in the Tx. However, there is always some variation between the array branches due to manufacturing tolerances, imperfections in board layout, and state-dependent variations in attenuation of the digitally controlled phase shifter. Moreover, due to defects caused by wire bonding (presumably, too much force was applied to bonding pads, causing small cracks on the die), our phase shifters caused larger amplitude imbalances than expected. Thus, almost 15 dB of measured small signal gain variation can be seen from Fig. 15 at 26.5 GHz between the best gain and the worst gain, when phase shifters are operating in their zero state. The average gain over all Rx channels is used as an equal gain reference for the measured imbalances. Similar behavior is observed also in other frequencies within the band. Certainly, such a large variation is not desired and will be corrected to the revised version of the transceiver.

Radiation patterns of all eight parallel 2×2 sub-arrays (antenna structure shown in Figs. 4 and 5) were measured in an antenna chamber by using A-info LB-28-15 standard gain horn antenna as a reference antenna. Stepper motors and angular shift were used to rotate the antenna under test (AUT) and Keysight N5247A PNA-X to measure the S_{21} between the horn antenna (connected to PNA port 1) and AUT ports (connected to PNA port 2) to each angle over the azimuth plane. The distance between the horn antenna and the AUT was set to 1.5 m. Full S-parameter calibration was performed up to the antenna

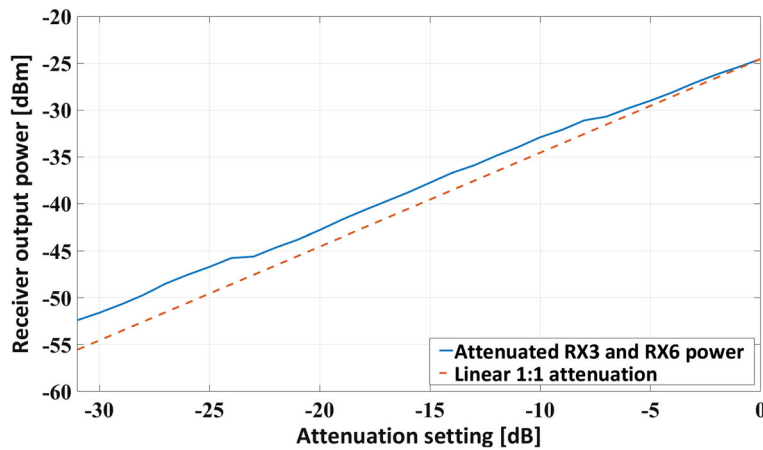


Fig. 13 Measured attenuator linearity compared to the ideal curve

connectors, and the known radiation pattern of the horn antenna was extracted out from the measurement data in post-processing. By summing together all the measured S_{21} values of the sub-arrays, we can extract the full array pattern.

Each transceiver board having eight RF chains will be connected to one 1×8 phased array (one row in Fig. 5). By extracting the measurement data from the gains of the Rx channels and array pattern data from the antenna array, we calculated the active array pattern. The extracted active array patterns with and without the gain imbalance shown in Fig. 15 is presented in Fig. 16. It can be seen that even a large gain imbalance has no significant effect on

the gain or to the width of the main lobe of the radiation pattern. Measured amplitude imbalance may even reduce the level of the first side lobe of the antenna array, as marked with the arrows in the figure. However, the third side lobe is significantly higher with measured gain imbalances compared to the situation where the average gain is used to calculate the antenna pattern. It is expected that with larger arrays, gain imbalance has even less impact as the large variations are averaged out with the number of antennas. In future work, the effects of amplitude imbalance and errors in phase progression over the antenna elements will be studied experimentally with active array measurements.

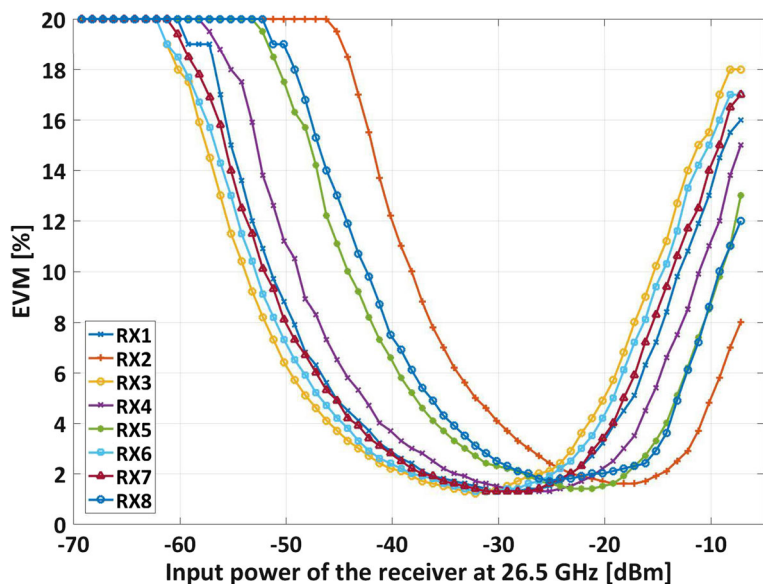
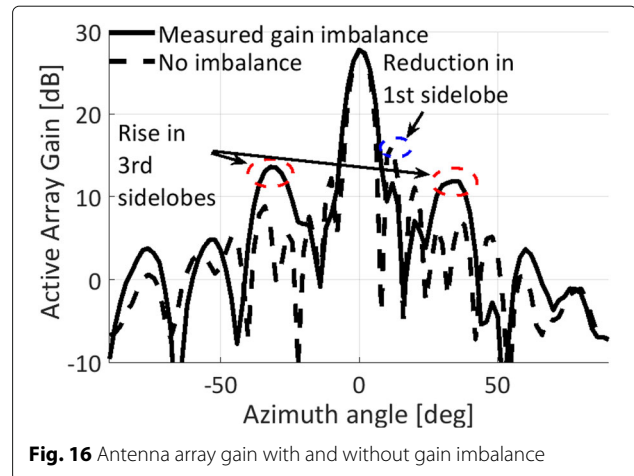
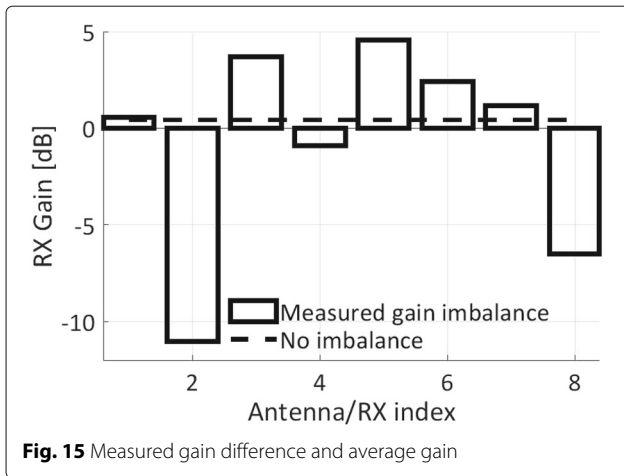


Fig. 14 Measured EVM vs signal power from all Rx channels



5.5 Transceiver power consumption

The RF board requires several separate supply voltages and linear low noise voltage regulation for sensitive analog components. The GaN PAs on our transceiver consume the largest amount of power of all of the components on the board. They are class AB devices, i.e., increasing the RF signal level also increases the drain current. They use a 20-V drain supply and a negative gate bias. The synthesizer requires 5 V and 3.3 V supplies, the LNA and the mixer require 3.3 V. The RF switches operate with -15 V (on-state) and 4 V (off-state) supplies. The attenuator requires 5 V and -5 V supplies.

PA gate biasing, attenuator and switches themselves consume very little power from the -5 V supply. Most of the -15 V power consumption is caused by the loss in the -5 V linear regulator. The phase shifters and the control logic use a 5 V supply, so that the phase shifters can be directly driven by the 5 V control logic. Control logic, LNA and attenuator supply voltages are regulated down from a 6 V supply. Power consumption breakdown is shown in Table 2. It can be seen that the PAs are responsible for approximately 83% of power consumption. The RF board was powered directly from laboratory power supplies.

Compared to other communication base station implementations, the proposed 5G transceiver operates at the RF output power class of microcell base stations [13].

6 Conclusions

Standardization of 5G is ongoing and due to this fact, standardized test signals for OFDM signal generation and demodulation for 5G mmW radios are not yet available. Therefore, we have used standard digital modulation test signals to test our design. EVM measurements indicate that the measured proof-of-concept 5G radio is capable of receiving wideband digitally modulated signals and can provide coherence gain when using two or more Rx channels. Measured radio Rx channels have at least 40 dB dynamic signal range and 30 dB attenuation dynamic range.

A phased array antenna may tolerate even large gain imbalances between the Rx channels. We have shown that even a relatively large imbalance between the Rx channels has no significant effect on the main receiving lobe of the antenna array. The amplitude imbalance may even attenuate some of the side lobes due to amplitude tapering.

Table 2 Estimated RF board power consumption at 30 dBm conducted RF output power per channel

	Supply voltage (V)	Current consumption (A)	Power consumption (W)	PAE (per PA)
Preamp 1	20	0.28	5.6	
Preamp 2	20	0.56	11.2	9%
8 PA array	20	6.4	128	12%
8 LNA array, Switches, LO gen, Control logic				
Mixer, RSSI, Attenuator	6	1.33	7.98	
Switches, PA biasing, Attenuator	-15	0.15	2.25	
Total power consumption			155	

Unfortunately, due to a stability problem with one of the PAs on the common amplifier path, we were unable to measure the performance of the Tx chain conclusively. We are designing a new version of our transceiver, which aims to fix this issue. In addition, gain control for the Tx side will be implemented so that the EIRP can be limited to comply with regulatory requirements.

Acknowledgements

The research leading to these results has received funding from the European Union H2020 5GPPP under grant no. 723247 and supported by the Institute for Information communications Technology Promotion (IITP) grant funded by the South Korea government (MSIP) (No.B0115-16-0001, 5GCHAMPION). Nédio Chrystian da Silva Neddef and Juho Rivinoja are gratefully acknowledged for their help with the measurements.

Authors' contributions

OK designed, simulated, and implemented the RF board with help from AP and TR. Measurements were carried out by ML, NT, and OK. OK made the cascade analysis. GD made the link budget calculations. MS designed, simulated, and measured the antenna board. The article was written by OK, ML, NT, and GD. The project was supervised by AP, AK, ST, and MP. All authors read and approved the final manuscript.

Competing interests

The authors declare that they have no competing interests.

Publisher's Note

Springer Nature remains neutral with regard to jurisdictional claims in published maps and institutional affiliations.

Author details

¹Centre for Wireless Communications, University of Oulu, Oulu, Finland.

²NOKIA, Oulu, Finland.

Received: 16 October 2017 Accepted: 30 July 2018

Published online: 15 August 2018

References

- M Mueck, EC Strinati, IG Kim, A Clemente, JB Dore, AD Domenico, T Kim, T Choi, HK Chung, G Destino, A Parssinen, A Pouttu, M Latva-aho, N Chuberre, M Gineste, B Vautherin, M Monnerat, V Frascolla, M Fresia, W Keusgen, T Haustein, A Korvala, M Pettissalo, O Liinamaa, in *2016 IEEE Globecom Workshops (GC Wkshps)*. 5G CHAMPION - rolling out 5G in 2018 (IEEE, 2016), pp. 1–6. <https://doi.org/10.1109/GLOCOMW.2016.7848798>
- B Sadhu, Y Tousei, J Hallin, S Sahl, S Reynolds, O Renström, K Sjögren, O Haapalahti, N Mazar, B Bokinge, G Weibull, H Bengtsson, A Carlinger, E Westesson, JE Thillberg, L Rexberg, M Yeck, X Gu, D Friedman, A Valdes-Garcia, in *2017 IEEE International Solid-State Circuits Conference (ISSCC)*. A 28GHz 32-element phased-array transceiver IC with concurrent dual polarized beams and 1.4 degree beam-steering resolution for 5G communication (IEEE, 2017), pp. 128–129. <https://doi.org/10.1109/ISSCC.2017.7870294>
- K Kibaroglu, M Sayginer, GM Rebeiz, in *2017 IEEE Radio Frequency Integrated Circuits Symposium (RFIC)*. An ultra low-cost 32-element 28 GHz phased-array transceiver with 41 dBm EIRP and 1.0-1.6 Gbps 16-QAM link at 300 meters (IEEE, 2017), pp. 73–76. <https://doi.org/10.1109/RFIC.2017.7969020>
- HT Kim, BS Park, SM Oh, SS Song, JM Kim, SH Kim, TS Moon, SY Kim, JY Chang, SW Kim, WS Kang, SY Jung, GY Tak, JK Du, YS Suh, YC Ho, in *2017 IEEE Radio Frequency Integrated Circuits Symposium (RFIC)*. A 28 GHz CMOS direct conversion transceiver with packaged antenna arrays for 5G cellular system (IEEE, 2017), pp. 69–72. <https://doi.org/10.1109/RFIC.2017.7969019>
- J Curtis, H Zhou, F Aryanfar, in *2016 IEEE MTT-S International Microwave Symposium (IMS)*. A fully integrated Ka-band front end for 5G transceiver (IEEE, 2016), pp. 1–3. <https://doi.org/10.1109/MWSYM.2016.7540314>
- YS Yeh, B Walker, E Balboni, B Floyd, A 28-GHz phased-array receiver front end with dual-vector distributed beamforming. *IEEE J. Solid State Circ.* **52**(5), 1230–1244 (2017)

- D-W Park, G-H Gwag, H-J Oh, I-m Park, Y-S Eo, in *2016 Asia-Pacific Microwave Conference (APMC)*. 28 GHz RF transceiver module for 5G beam-forming system (IEEE, 2016), pp. 1–4. <https://doi.org/10.1109/APMC.2016.7931278>
- 3GPP, NR; base station (BS) radio transmission and reception, 38.104, release 15. Technical specification (TS), 3rd Generation Partnership Project (3GPP) (2018). <http://www.3gpp.org/DynaReport/38104.htm>. Accessed 6 Aug 2018
- G Destino, O Kursu, S Tammelin, J Haukipuro, M Sonkki, T Rahkonen, A Pärssinen, M Latva-aho, A Korvala, M Pettissalo, in *2017 European Conference on Networks and Communications (EuCNC)*. System analysis and design of mmW mobile backhaul transceiver at 28 GHz (IEEE, 2017), pp. 1–5. <https://doi.org/10.1109/EuCNC.2017.7980768>
- T Tuovinen, N Tervo, A Pärssinen, in *2016 46th European Microwave Conference (EuMC)*. RF system requirement analysis and simulation methods towards 5G radios using massive MIMO (IEEE, 2016), pp. 142–45. <https://doi.org/10.1109/EuMC.2016.7824298>
- A Natarajan, SK Reynolds, MD Tsai, ST Nicolson, JHC Zhan, DG Kam, D Liu, YLO Huang, A Valdes-Garcia, BA Floyd, A fully-integrated 16-element phased-array receiver in SiGe BiCMOS for 60-GHz communications. *IEEE J. Solid State Circ.* **46**(5), 1059–1075 (2011)
- IEEE, IEEE standard for information technology–telecommunications and information exchange between systems local and metropolitan area networks–specific requirements - part 11: Wireless LAN medium access control (MAC) and physical layer (PHY) specifications. Std 802.11-2016 (Revision of IEEE Std 802.11-2012), IEEE, 1–3534 (2016)
- G Auer, V Giannini, C Desset, I Godor, P Skillermark, M Olsson, MA Imran, D Sabella, MJ Gonzalez, O Blume, A Fehske, How much energy is needed to run a wireless network? *IEEE Wirel. Commun.* **18**(5), 40–49 (2011)

Submit your manuscript to a SpringerOpen® journal and benefit from:

- Convenient online submission
- Rigorous peer review
- Open access: articles freely available online
- High visibility within the field
- Retaining the copyright to your article

Submit your next manuscript at ► springeropen.com